Matter

CellPress

Article

Unraveling the Impact of Halide Mixing on Crystallization and Phase Evolution in $CsPbX_3$ Perovskite Solar Cells

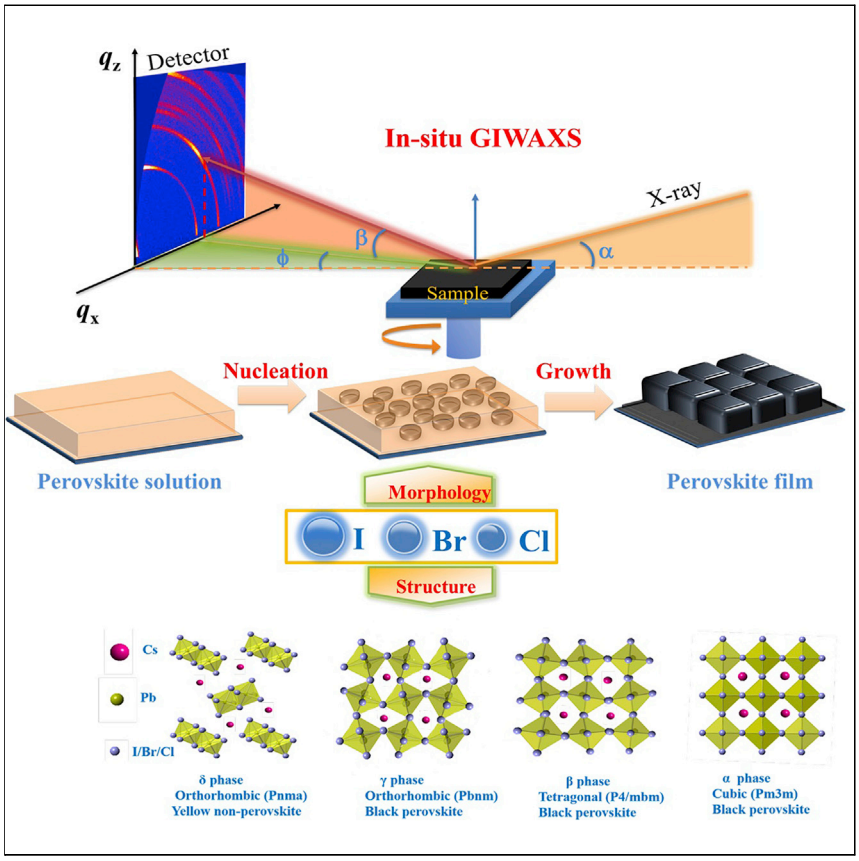

A fundamental understanding of the all-inorganic perovskite film-formation kinetics and phase-transition mechanism is revealed by *in situ* GIWAXS. Our work demonstrates the power of ternary halide engineering to obtain high-quality all-inorganic perovskite films with enhanced phase stability.

Junjie Ma, Minchao Qin, Yuhao Li, ..., Yichu Wu, Guojia Fang, Xinhui Lu

gjfang@whu.edu.cn (G.F.)
xinhui.lu@cuhk.edu.hk (X.L.)

HIGHLIGHTS

GIWAXS is utilized to probe real-time phase evolution of $CsPbX_3$ perovskite film

The role of halide elements in phase evolution is revealed

High-quality perovskite film is obtained by ternary halide engineering

A PCE as high as 17.14% is achieved

Ma et al., Matter 4, 313–327
January 6, 2021 © 2020 Elsevier Inc.
https://doi.org/10.1016/j.matt.2020.10.023

3 **Understanding**
Dependency and conditional studies on material behavior

Matter

CellPress

Article

Unraveling the Impact of Halide Mixing on Crystallization and Phase Evolution in $CsPbX_3$ Perovskite Solar Cells

Junjie Ma,[1,2,3] Minchao Qin,[1,3] Yuhao Li,[1] Xiao Wu,[1] Zhaotong Qin,[1] Yichu Wu,[2] Guojia Fang,[2,*] and Xinhui Lu[1,4,*]

SUMMARY

All-inorganic perovskite solar cells (PSCs) have attracted wide attention for their excellent thermal stability. However, the detailed crystallization process and complicated phase-transition mechanism of the $CsPbX_3$ film with different halide compositions (I, Br, Cl) remain mysterious. In this study, systematic investigations are performed via state-of-art *in situ* grazing-incidence wide-angle X-ray scattering to understand the role of the halide elements in all-inorganic perovskite crystallization kinetics, phase-transition, and stabilization mechanism as well as how film morphology and grain size are affected. Based on these results, we were able to fabricate high-performance ternary halide (I, Br, Cl) all-inorganic PSCs through a precise compositional engineering. Our results provide guidance for an in-depth understanding of all-inorganic perovskite materials and pave the way to obtain high-performance all-inorganic PSCs.

INTRODUCTION

Recently, organic-inorganic hybrid lead halide perovskite solar cells (PSCs) have achieved rapid progress with power-conversion efficiencies (PCEs) of over 25% due to their outstanding optoelectronic properties.[1,2] However, organic-inorganic perovskite materials possess intrinsic thermal stability issues due to the employment of highly volatile organic components such as methylammonium cation (MA^+) or formamidinium cation (FA^+) under persistent attacks by heat.[3] On the contrary, all-inorganic PSCs exhibit improved thermal stability by replacing unstable organic cations with relatively stable inorganic cesium (Cs^+) cation, and the record PCE has been pushed from 2.9% to over 18% in recent years.[4] Besides thermal stability, the largely tunable optical band gap (1.7–2.3 eV) of $CsPbX_3$ offers a wide application of all-inorganic PSCs, such as being the top cell in tandem devices and semitransparent solar cells.[5,6,7]

Due to the lattice distortion caused by the relatively small size of Cs^+ as an A-site cation, two other photoactive phases including β phase (tetragonal, P4/mbm) and γ phase (orthorhombic, Pbnm) have been reported,[8,9] besides the most symmetric α phase (cubic, Pm3m) for all-inorganic perovskite $CsPbX_3$ (Figure 1A), which significantly complicate the film-formation and crystallization pathways. Zhang et al. investigated the influence of solvent composition (volume ratio of dimethyl sulfoxide [DMSO]/*N*,*N*-dimethylformamide [DMF]) on the morphology and quality of $CsPbI_2Br$ film using scanning electron microscopy (SEM).[10] They pointed out that the volatilization rate and viscosity of solvent are important factors that affect the film-formation process. Chen et al. revealed the synergistic effect of gradient

Progress and Potential

All-inorganic perovskites have attracted increasing attention because of their potentially better thermal stability. However, the film-formation process and phase-transition mechanism of all-inorganic perovskite are still unclear. There is no consensus regarding the role of halide elements in the phase-transition and crystal growth kinetics of all-inorganic perovskite.

In this work, state-of-the-art *in situ* grazing-incidence wide-angle X-ray scattering is utilized to probe real-time crystalline and phase evolution of all-inorganic perovskite film. The roles of I, Br, and Cl in phase-transition and crystallization kinetics are revealed individually and correlated with device performance of all-inorganic perovskite solar cells, which leads to the development of a facile and brand-new means to fabricate highly efficient and phase-stable ternary halide (I, Br, Cl) all-inorganic perovskite solar cells.

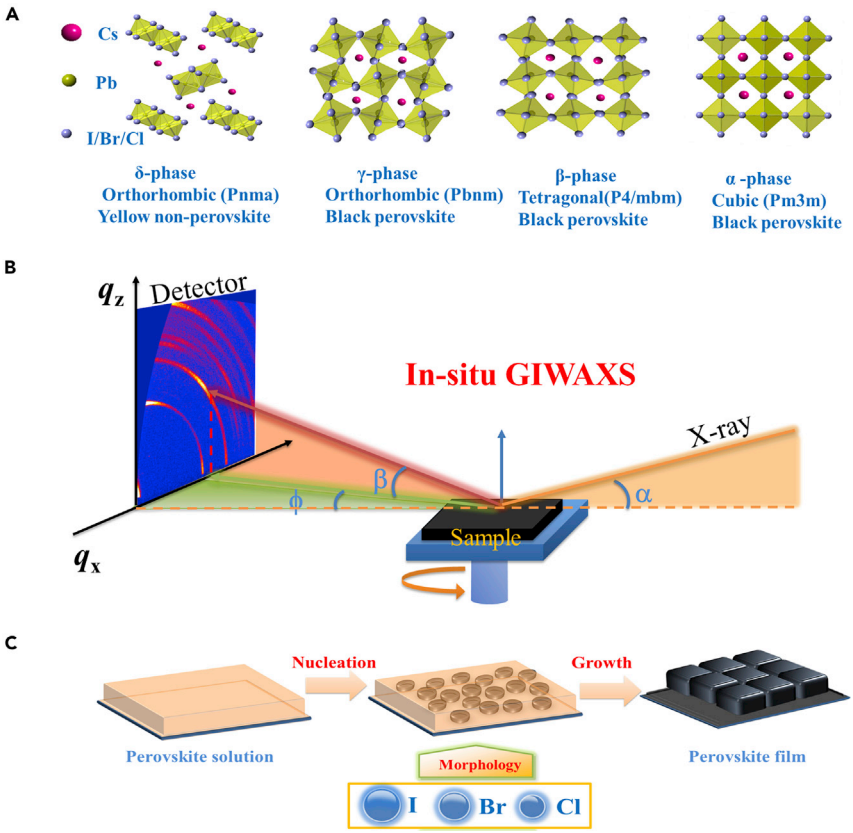

Figure 1. Investigation of the Role of the Halide Elements in All-Inorganic Perovskite Crystallization and Phase-Transition Process via GIWAXS Characterization

(A) Cartoon of all-inorganic perovskite crystal structures of commonly formed phases (α, β, γ, δ).

(B) Schematics of *in situ* GIWAXS characterization.

(C) Schematics of perovskite film-formation procedures.

thermal annealing and antisolvent on $CsPbI_2Br$ film formation.[11] Jiang et al. presynthesized DMSO Lewis base adducts to promote the growth of all-inorganic perovskite film with low activation energy. These Lewis base adducts can efficiently prevent the rapid reaction of precursors and slow down the crystal growth. Thus, a high-quality perovskite film can be fabricated under low temperatures.[12] Wang et al. developed the solvent-controlled growth method to produce high-quality all-inorganic perovskite thin films. They left the precursor films in the nitrogen-filled glovebox for several tens of minutes before annealing. The residual DMSO enhanced the mass transport and diffusion and slowed down the evaporation rate of the solvent, which is beneficial for film quality.[7] To date, studies on solution chemistry and crystallization mechanism of all-inorganic perovskites are still very limited. *In situ* grazing-incidence wide-angle X-ray scattering (GIWAXS) characterization is an effective means by which to understand the perovskite film-formation mechanism. Liu et al. proposed the *in situ* observation of vapor-assisted 2D-3D perovskite heterostructure formation process. They found that the 3D-to-2D transformation of MAPbI3 is initiated by butylamine vapor.[13] Szostak et al. explored the formation of formamidinium-based perovskite by the antisolvent method during spin-coating through *in situ* GIWAXS. They identified various crystalline phases and provided guidelines to manage the composition during film processing.[14] Fan et al. performed *in situ* GIWAXS measurements to study the structural evolution of

[1]Department of Physics, The Chinese University of Hong Kong, Shatin 999077, Hong Kong

[2]School of Physics and Technology, Wuhan University, Wuhan 430072, People's Republic of China

[3]These authors contributed equally

[4]Lead Contact

*Correspondence: gjfang@whu.edu.cn (G.F.), xinhui.lu@cuhk.edu.hk (X.L.)

https://doi.org/10.1016/j.matt.2020.10.023

all-inorganic perovskite films blade-coated at different processing temperatures.[15] Our group has investigated the organic-inorganic hybrid perovskite crystallization pathway by *in situ* GIWAXS, revealing the important role of Cs^+ in extending the annealing window.[16] However, *in situ* studies on all-inorganic perovskites are still very limited. The underlying phase-evolution and film-formation mechanisms remain mysterious to date.

Furthermore, phase-stability and phase-change mechanisms remain a major challenge for all-inorganic PSCs.[17,18] The desired black perovskite phases (α phase, β phase, γ-phase, Figure 1A) are thermally unstable and could spontaneously transform to the yellow non-photoactive orthorhombic phase (δ phase) under ambient conditions.[19,20] Sutton et al. investigated the structural transitions and thermodynamic stability of various polymorphs of $CsPbI_3$ and showed that the orthorhombic polymorph is the most stable phase among these polymorphs, but it remains less stable than the yellow non-perovskite phase.[21] Marronnier et al. studied the competition between all the low-temperature phases of $CsPbI_3$ (γ, δ, β) using total energy and vibrational entropy calculations and highlighted that avoiding the order-disorder entropy term arising from double-well instabilities is a key to preventing the formation of the yellow δ phase.[9] To hinder the unwanted phase transition, Swarnkar et al. introduced organic phenylethylammonium iodide (PEAI) additives into perovskite.[22] Substituting Pb^{2+} ions with smaller metal ions such as Ge^{2+}, Eu^{3+}, and Mn^{2+} have been developed to enhance the phase stability.[23]

Regulating the halide component by introducing Br and Cl has been proved to be a viable route to improve the PSCs' stability.[24,25] Researchers devoted extensive efforts to reveal the effect of halide on the organic-inorganic hybrid perovskite system. Hieulle et al. unraveled the impact of halide mixing on organic-inorganic hybrid perovskite stability. By combining scanning tunneling microscopy and density functional theory, they determined the optimal Cl incorporation ratio for stability increase without detrimental band-gap modification.[26] Fan et al. elucidated the role of chlorine in $MAPbI_3$ perovskite. They demonstrated that the formation of a porous PbCl scaffold in the precursor film induced high-quality perovskite realization.[27] Cheng et al. reported triple-anion $CH_3NH_3PbI_{2-x}BrCl_x$ perovskite film. They pointed out that the involvement of both bromide and chloride could suppress the trap states and non-radiative recombination loss.[28] Compared with the organic-inorganic hybrid perovskite system, all-inorganic perovskites process different compositions and thereby distinct film-formation processes, which require further exploration. However, to date there is no consensus regarding the role of halide elements including I, Br, and Cl in phase transition and crystal growth kinetics accompanied by device photovoltaic performance in all-inorganic perovskites.

Last but not least, the fabrication of high-performance all-inorganic PSCs still mainly relies on the assistance of organic additives. Lau et al. reported a cation exchange growth method for fabricating all-inorganic perovskite $CsPbI_3$ during the black perovskite phase by adding methylammonium iodide additives to the precursor.[29] In addition, organic salts such as dimethylammonium iodide (DMAI) are commonly used to assist the crystal growth of all-inorganic perovskite in order to fabricate a stable device with PCEs of over 18%.[30] However, the employment of DMAI requires an additional presynthesis procedure and often leads to conditions of iodine excess, challenging the precise control of halide composition.[31] Therefore, developing new strategies for high-performance all-inorganic PSCs without the assistance of organic salts is still highly desirable.[32]

In this work, we carried out systematic synchrotron-based *in situ* GIWAXS measurements to investigate the influence of ternary halide mixing on the film crystallization mechanism and phase evolution of all-inorganic perovskite $CsPbX_3$ (X = I, Br, Cl) under spin-coating (Figure 1B).[16] Benefiting from the guidance of the *in situ* GIWAXS, we were able to deeply understand the all-inorganic perovskite film-formation and phase-transition mechanisms and construct high-quality all-inorganic perovskite films with enhanced phase stability based on ternary halide engineering via precise regulation of crystallization kinetics. We found that pure $CsPbI_3$ exhibits the broadest absorption spectrum but the worst film coverage due to the highest phase-formation barrier. Besides, the black phase of $CsPbI_3$ is unstable owing to the large deviation of the tolerance factor from the cubic phase range.[24] Introducing Br ions not only compensates the lattice distortion caused by the small Cs^+ but also significantly expedites the nucleation and crystal growth rate, simultaneously improving the film coverage and phase stability. However, it also causes reduction of the average grain size as well as the photocurrent due to band-gap enlargement. Remarkably, the doping of Cl can improve the film crystallinity and crystalline orientation. However, it further deviates the band gap from the optimized value. Therefore, by balancing the band gap, nucleation, and crystal growth rates through fine-tuning the I/Br/Cl ratio (Figure 1C), devices with a conventional I/Br ratio of 2:1 have achieved a PCE as high as 15.04% under reverse voltage scanning. Remarkably, a new halide composition of I/Br = 4:1 has obtained a record high PCE of 17.14% with only 0.6 eV energy loss (E_{loss}) under reverse voltage scanning, which is to our knowledge the highest PCE reported for all-inorganic PSCs based on pure all-inorganic perovskite precursors without the assistance of organic additives to date.[33]

RESULTS AND DISCUSSION

To uncover the impact of mixing I and Br in the phase evolution, we carried out *in situ* GIWAXS characterization during the film formation of $CsPb(I_{1-x}Br_x)_3$ (x = 0%, 20%, 33%, 50%, 66%) during the spin-coating process. Different compositions of halide mixture were prepared by mixing pure inorganic CsI, PbI_2, and $PbBr_2$ with specific molar ratios in DMF/DMSO. False-color GIWAXS intensity maps versus q_z and frame numbers (3 s per frame) of $CsPb(I_{1-x}Br_x)_3$ (x = 0%, 20%, 33%, 50%, 66%) films are shown in Figures 2A–2E. The corresponding intensity profiles along the q_z direction are presented in Figures S1A–S1E. The X-ray diffraction (XRD) standard patterns and characteristic diffraction peaks to distinguish α, β, γ, and δ phases are displayed in Figure S2.

For the 0% Br film (Figure 2A), crystallization began at about the 52nd frame with the yellow δ phase scattering peaks appearing first at 0.71 $Å^{-1}$, after which the black γ phase at 1.02 $Å^{-1}$ and 1.15 $Å^{-1}$ appeared at the 66th frame. For the 20% Br film (Figure 2B), the dominant black phase became β phase as indicated by the scattering peaks at 1.03 $Å^{-1}$ and 2.35 $Å^{-1}$, consistent with the fact that Br^- could correct the tolerance factor to some extent and thereby experience less distortion in the corner-sharing of PbX_6 octahedra. Moreover, the β phase appeared at the 58th frame, slightly earlier than the δ phase which appeared at the 70th frame. For the 33% Br film (Figure 2C), the scattering peak for black α phase can be clearly identified at 1.04 $Å^{-1}$ starting from the 46th frame, while the δ phase appeared at the 92nd frame. When the concentration of Br further increased, to 50% and 66%, the appearance of black α phase was further advanced without the detection of δ phase during the whole spin process (Figures 2D and 2E). The emergence time (frame number) of the black perovskite phase and yellow non-perovskite phase versus different Br components are summarized in Figure 2F. An obvious trend of black phase advancing

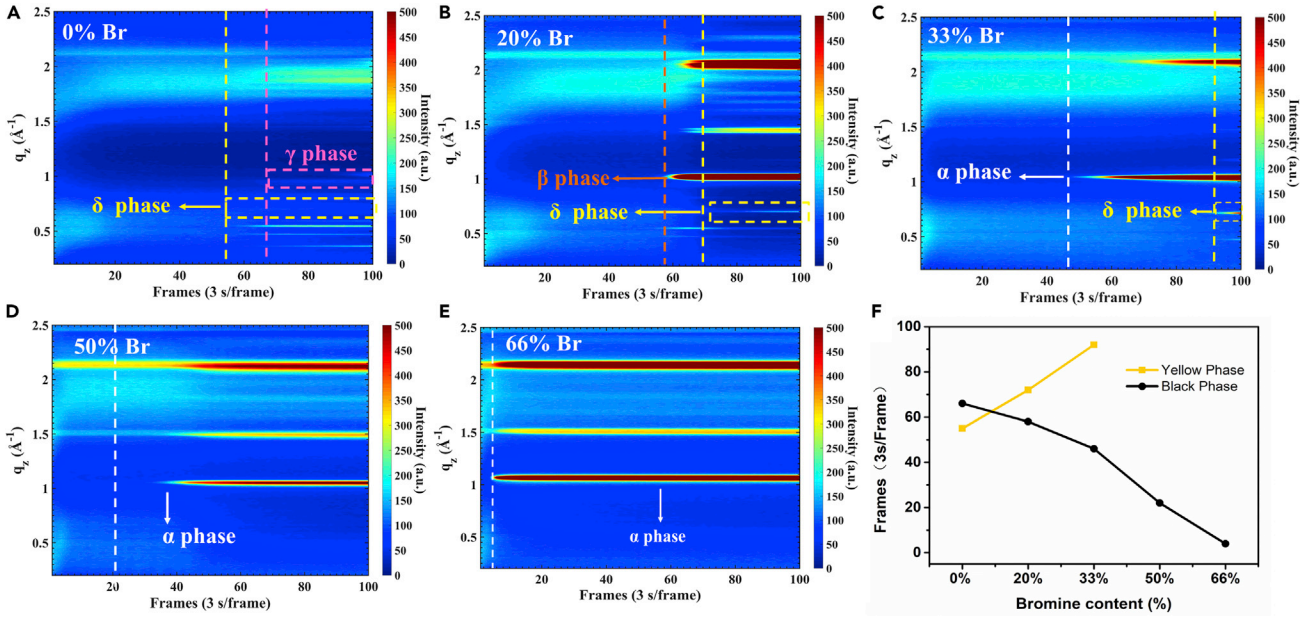

Figure 2. Time-Resolved GIWAXS Profile Analysis of All-Inorganic Perovskites with Different I/Br Ratios

(A–E) Time evolution of false-color intensity maps versus q_z for $CsPbI_3$ (A), $CsPb(I_{0.8}Br_{0.2})_3$ (B), $CsPb(I_{0.67}Br_{0.33})_3$ (C), $CsPb(I_{0.5}Br_{0.5})_3$ (D), and $CsPb(I_{0.34}Br_{0.66})_3$ (E).

(F) Emergence frame number of the photoactive black phase and photoinactive yellow phase in $CsPb(I_{1-x}Br_x)_3$ (x = 0%, 20%, 33%, 50%, 66%) films.

and yellow phase deferring can be observed, suggesting that Br ions play an important role in facilitating the formation of the black perovskite phase and effectively suppress the unwanted phase transition to the yellow δ phase. It was reported that the rattling of Cs, low number of Cs-I contacts, and high degree of octahedral distortion cause instability of all-inorganic perovskite.[34] This suggests that the incorporation of Br ions, with relatively stronger electronegativity and smaller ionic size than those of I ions, could form stronger coordination of Cs ions and reduce the octahedral distortion, which would effectively contribute to the stabilization of the black phase.

The time evolution of the scattering peak area at $q_z \approx 1$ Å^{-1} for $CsPb(I_{1-x}Br_x)_3$ (x = 0%, 20%, 33%, 50%, 66%) perovskites are plotted in Figures 3A–3E to aid in further understanding the nucleation and crystal growth kinetics. Three stages of crystallization can be identified: (I) solution stage; (II) nucleation and fast growth stage; (III) slow growth stage. The mechanism of nucleation and crystal growth in the film-formation process can be explained by the LaMer theory.[35,36] As shown in Figure 3G, the crystallization starting points are gradually advanced with the increase of Br concentration. It is suggested that the incorporation of more Br could lower the nucleation barrier of the perovskite phase so as to enter stage II of nucleation and fast growth earlier. The nucleation and fast growth process quickly consume the solute concentration. The crystallization process moves into the third crystallinity saturation stage (stage III) when the nucleation stops and the crystal growth slows down. For the 0% Br film that enters stage II at the latest, the nucleation sites are too scarce to form a fully covered film. A smaller Br content gives rise to a milder supersaturation condition, leaving sparser nucleation sites for further crystal growth in stage II. Comparing the 20% and 33% Br films, their time spent in stage II is similar while the 20% film experiences much milder supersaturation conditions with fewer nucleation sites when entering stage III. Figure 3F is a cartoon that qualitatively

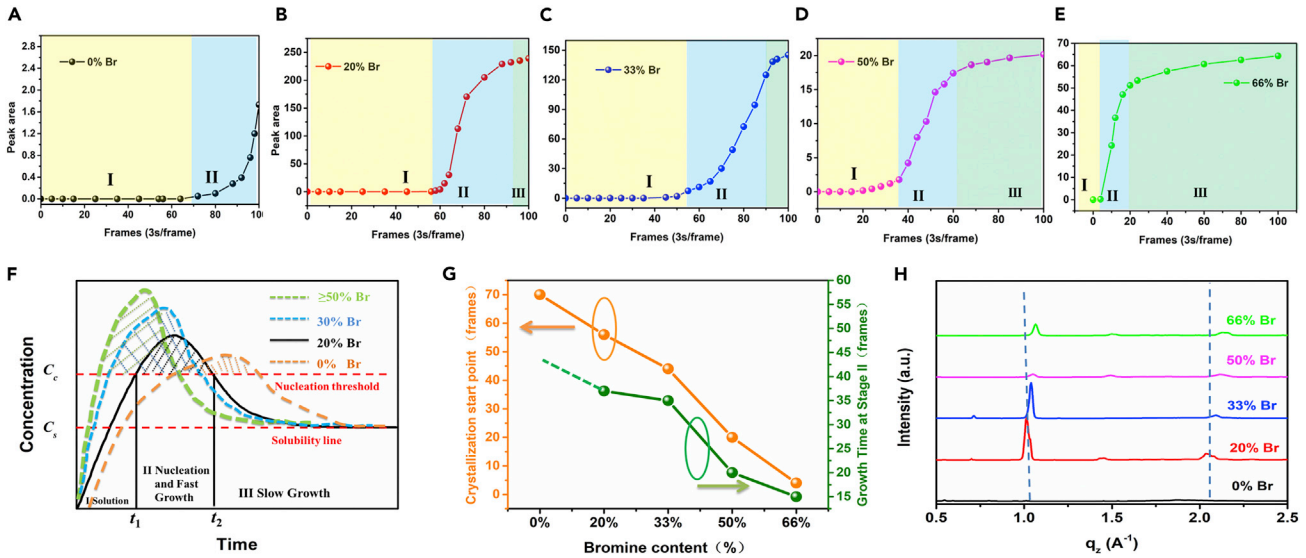

Figure 3. Crystallization Process Analysis of All-Inorganic Perovskites with Different I/Br Ratios

(A–E) Time evolution of peak area of the $CsPb(I_{1-x}Br_x)_3$ (x = 0% [A], 20% [B], 33% [C], 50% [D], 66% [E]) perovskites.

(F) Classical Lamer diagram for monodispersed particle formation. C_s is the solubility, C_c is the minimum concentration for nucleation.

(G) Evolution of crystallization starting point (no. of frames) and crystal growth time at stage II of $CsPb(I_{1-x}Br_x)_3$ (x = 0%, 20%, 33%, 50%, 66%) films.

(H) Summary of intensity profiles along the q_z direction for the $CsPb(I_{1-x}Br_x)_3$ (x = 0%, 20%, 33%, 50%, 66%) films at the last (100^{th}) frame.

summarizes the influence of halide content on the nucleation and crystal growth (Figures 3A–3E), based on the classical LaMer theory for monodispersed particle formation. When the Br concentration is increased from 33% to 66%, the launch time of stage II is further advanced, which is compensated by the shortening of the duration of stage II, giving rise to a similar amount of nucleation sites. The corresponding intensity profiles along the q_z direction (out-of-plane) were extracted in detail (Figure 3H). The diffraction peak gradually shifts to higher q values with more Br in the film, confirming that Br indeed entered the lattice in substitution of I, inducing the lattice shrinkage to stabilize the perovskite crystal structure.[37]

The film morphology of $CsPb(I_{1-x}Br_x)_3$ (x = 0%, 20%, 33%, 50%, 66%) was further studied by SEM, shown in Figures 4A–4E and S3. All the films were annealed under the same temperature conditions as detailed in Experimental Procedures. The corresponding statistics of the grain-size distribution are shown in Figures 4F–4J. The 0% Br film exhibits dendrite morphology with observable pinholes, which originate from the very small amount of nucleation sites and a high crystallization barrier, which hinders the crystal growth. The introduction of Br ions can significantly alter the morphology of the resultant film. A continuous coverage of the film can be obtained, owing to the formation of sufficient nucleation sites promoted by the incorporation of Br. The variation in morphology versus the concentration of Br is in accordance with the crystallization kinetics observed by the *in situ* data. For the 20% Br film, mild nucleation leads a compact morphology with very large grains. In contrast, the 33% and higher Br films present compact morphology with much smaller grain sizes due to the relatively faster nucleation process. Notably, when the Br concentration is further increased to 66%, the pinholes appear again. We speculate that too rapid nucleation would restrain the crystal continuous growth and result in pinholes during the film-formation process. Hence, it is suggested that precisely regulating the crystallization kinetics is critical to the resultant film morphology. Figure 4K presents the ultraviolet-visible (UV-vis) absorption spectra of films with different Br

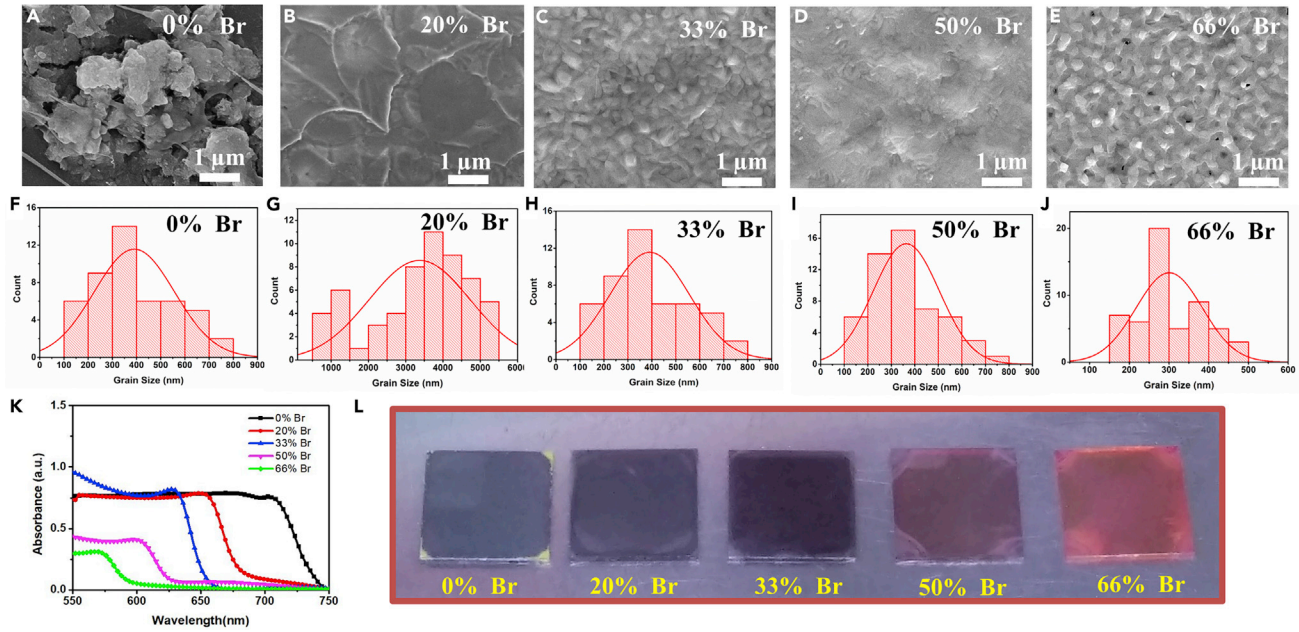

Figure 4. Morphology and Optical Absorption Property of All-Inorganic Perovskites with Different I/Br Ratios

(A–E) Top-view SEM images of the $CsPb(I_{1-x}Br_x)_3$ (x = 0% [A], 20% [B], 33% [C], 50% [D], 66% [E]) perovskites after annealing. Scale bar: 1 μm.

(F–J) Grain-size distribution histograms of the $CsPb(I_{1-x}Br_x)_3$ (x = 0% [F], 20% [G], 33% [H], 50% [I], 66% [J]) films.

(K) UV-vis absorption spectra of the $CsPb(I_{1-x}Br_x)_3$ (x = 0%, 20%, 33%, 50%, 66%) films.

(L) Photographs of $CsPb(I_{1-x}Br_x)_3$ (x = 0%, 20%, 33%, 50%, 66%) films.

concentrations. The absorption edges blue-shift noticeably with the increase of Br, demonstrating its powerful band-gap-tuning ability.[38] This is consistent with the appearance of film color (Figure 4L), which gradually turns lighter and becomes semitransparent with the increase of Br.

Further investigations on the influence of chlorine doping were performed with *in situ* GIWAXS. A small amount (2%) of the $CsPbICl_2$ precursor was added to $CsPb(I_{0.67}Br_{0.33})_3$ precursor, which was denoted as $CsPb(I_{0.67}Br_{0.33})_3$:Cl. Note that here, $CsPbICl_2$ was used to introduce Cl instead of $CsPbCl_3$, because it is very difficult to dissolve CsCl in the DMF/DMSO solution due to the low solubility. We prepared $CsPbICl_2$ precursor by dissolving CsI and $PbCl_2$ in mixed solvent DMSO/DMF solution and retained the demanded stoichiometric ratio of Cs and Pb. Due to the small amount added, changes in the I/Br ratio are considered negligible, which was confirmed by UV-vis absorption spectra (Figure S6A). Compared with the film without Cl, the perovskite film with Cl presents an earlier launch of nucleation (Figures 5A and 5B) and a deferred growth rate with higher crystallinity, as indicated by the integral area of the (100) scattering peak (Figure 5C). Two-dimensional (2D) GIWAXS patterns of the film with and without Cl are shown in Figures 5D and 5E. Both films exhibit preferred orientation with the (100) planes parallel to the substrates, implied by the (100) diffraction peaks concentrated along the q_z axis. The film with Cl shows a much better orientational order with a narrower full width at half maximum of the polar intensity profile of the (110) peak (Figure 5F). The 2D GIWAXS patterns of $CsPb(I_{0.67}Br_{0.33})_3$:$Cl_x$ (x = 0%, 0.25%, 0.5%, 1%) films are shown in Figure S4. It is suggested that the addition of Cl could promote the cubic phase formation, giving rise to films with enhanced crystallinity and orientational order.

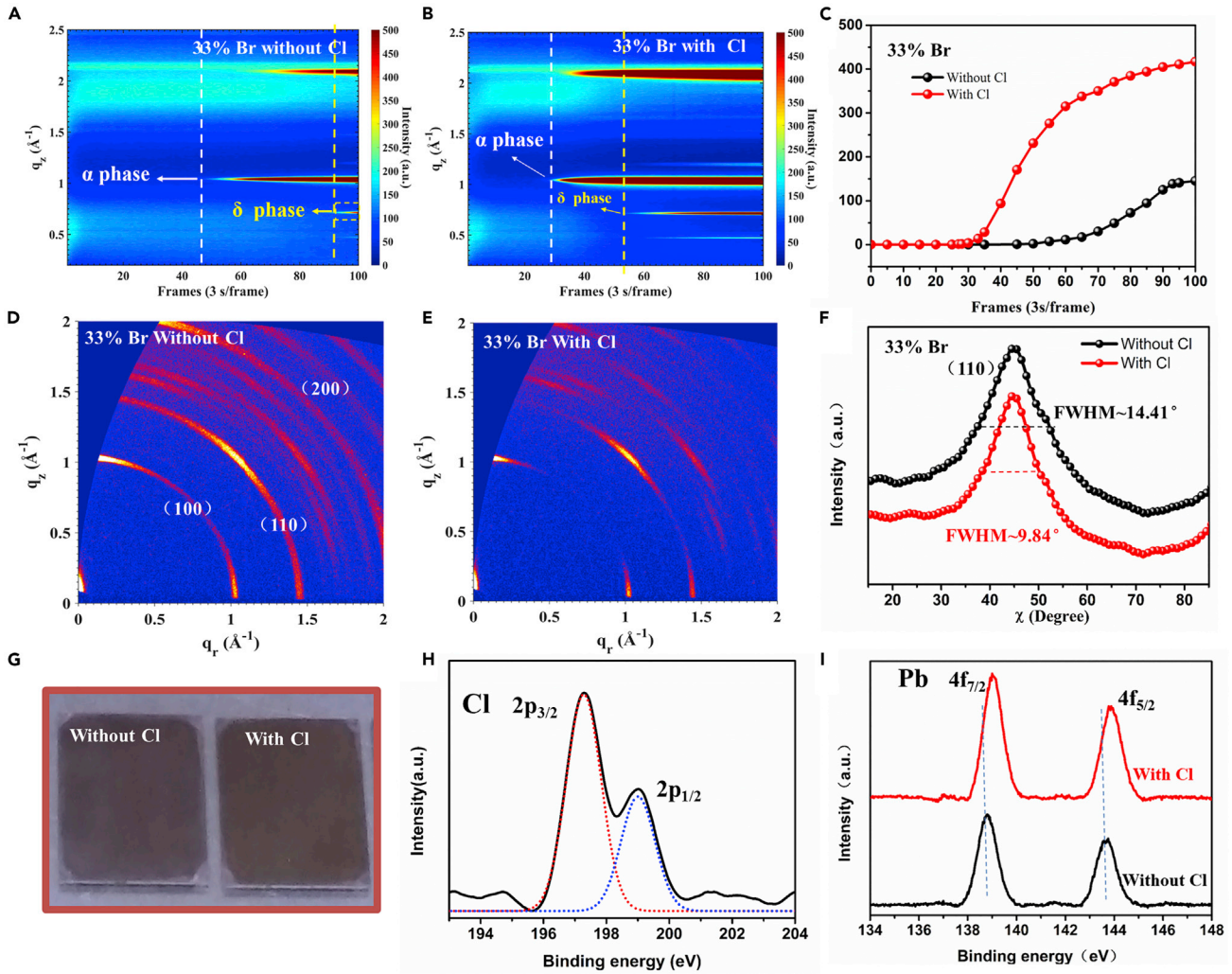

Figure 5. Effect of Cl Element on All-Inorganic Perovskite Crystallization Process and Microstructure

(A and B) False-color intensity maps versus q_z and the frame numbers for the $CsPb(I_{0.67}Br_{0.33})$ film without Cl (A) and with Cl (B).

(C–E) Peak areas of the cubic (100) phase as a function of the frame numbers for the corresponding films without and with Cl (C). 2D GIWAXS patterns of the $CsPb(I_{0.67}Br_{0.33})_3$ film without Cl (D) and with Cl (E) after annealing.

(F) Polar intensity profiles along the (110) plane in the q range of 1.4–1.5 $Å^{-1}$ of the $CsPb(I_{0.67}Br_{0.33})$ film with and without Cl. FWHM, full width at half maximum.

(G) Photographs of $CsPb(I_{0.67}Br_{0.33})$ film with and without Cl addition.

(H) XPS spectra of Cl 2p of the $CsPb(I_{0.67}Br_{0.33})_3$:Cl film.

(I) XPS spectra of Pb 4f of the $CsPb(I_{0.67}Br_{0.33})_3$ films with and without Cl.

X-ray photoelectron spectroscopy (XPS) measurements further confirmed the successful incorporation of Cl into the resultant films (Figure 5H). It can be estimated that the Pb/Cl ratio in the perovskite film is 1:0.05 by analyzing the intensity ratio of Pb and Cl from XPS element core-level energy spectra. We also analyzed the intensity profiles along the q_z direction from the GIWAXS measurement for perovskite film with and without Cl (Figure S13). The monotonic shift of the peaks to larger q values after introducing Cl further indicates the shrinkage of the crystalline lattice, which suggests that Cl enters the crystal lattice. Theoretical calculation pointed out that Cl tends to substitute Br in the lattice.[26] The spin-orbital doublet peaks of Pb ($4f_{7/2}$ $4f_{5/2}$) slightly shifted to stronger binding energy with the addition of Cl (Figure 5I), which is ascribed to the higher electronegativity of Cl, corresponding with

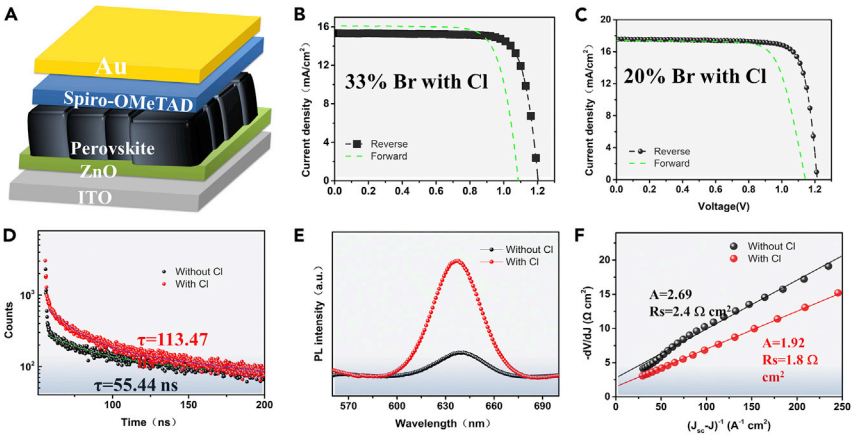

Figure 6. Photovoltaic Property Characterizations of the Devices

(A) Schematic view of the device structure.

(B and C) *J-V* curves of the best-performing device based on $CsPb(I_{0.67}Br_{0.33})$:Cl (B) and $CsPb(I_{0.80}Br_{0.20})$:Cl (C) perovskite film measured under reverse(forward) voltage scanning.

(D) Steady-state PL.

(E) TRPL decay curves.

(F) Plots of $-dV/dJ$ versus $(J_{sc} - J)^{-1}$ and the corresponding linear fitting curves of the devices with and without Cl addition.

the enhanced crystallinity and orientational order.[28] In brief, the film with Cl exhibited better orientation order and crystallinity, which could be attributed to the perovskite lattice reconstruction and the modulation of crystallization kinetics during the perovskite film-formation process.

The XPS survey scan is shown in Figure S5. UV-vis absorption spectra of $CsPb(I_{0.67}Br_{0.33})$:Cl_x (x = 0%, 0.25%, 0.5%, 1%, 2%) films exhibited a slight blue-shift with increased Cl concentrations (Figure S6A).[39] Both films display mirror-like surfaces (Figures 5G and S6B). The corresponding surface morphology was characterized by SEM (Figures S6C–S6G). The film with Cl exhibits more compact and homogeneous crystal domains.

Based on the understanding of film morphology and crystallization behaviors, we fabricated planar PSCs with a structure of indium tin oxide (ITO)/ZnO/perovskite/Spiro-OMeTAD/Au (Figure 6A) for the two film compositions with the best film quality: $CsPb(I_{0.67}Br_{0.33})_3$:Cl and $CsPb(I_{0.80}Br_{0.20})_3$:Cl. The cross-section SEM image of the entire device is shown in Figure S10. The corresponding energy diagrams based on literature are shown in Figure S11.[40,41] The champion PSC with reverse voltage scanning based on $CsPb(I_{0.67}Br_{0.33})_3$:Cl shows an open-circuit voltage V_{oc} of 1.21 V, a short-circuit current density J_{sc} of 15.62 mA cm^{-2}, and a fill factor (FF) of 79.39%, yielding a PCE of 15.02%, which is slightly better than previously reported results (Figure 6B).[42] For the $CsPb(I_{0.80}Br_{0.20})_3$:Cl film with the same device structure, a champion PCE of 17.14% with a V_{oc} of 1.21 V, a J_{sc} of 17.57 mA cm^{-2}, and FF of 80.36% was achieved (Figure 6C). To our knowledge, this is the best PCE using pure inorganic precursors without the assistance of organic additives reported so far.[43] The detailed photovoltaic parameters of the best-performing device based on $CsPb(I_{0.67}Br_{0.33})$:Cl and $CsPb(I_{0.80}Br_{0.20})$:Cl perovskite under reverse(forward) voltage scanning are summarized in Tables S4 and S5, respectively. We noted that the 33% Br and 20% Br gave the same V_{oc} although they have different band gaps. We attribute this to the smaller non-radiative recombination losses due to

the higher perovskite film quality of the 20% Br device. From Figures 4B and 4C, it is obvious that the 20% Br perovskite exhibits a better film quality with larger grain size and fewer grain boundaries compared with the 33% Br perovskite, which will reduce the trap states and suppress the non-radiative recombination, thus contributing to larger V_{oc} values.[44] Besides, the 20% Br film exhibits a better energy-level alignment between perovskite and Spiro-OMeTAD (Figure S11), facilitating the injection of holes and reducing the interface recombination, which is also beneficial to a higher V_{oc}. The device parameter statistics of the devices with different Cl compositions are shown in Figures S7 and S8 and Tables S1 and S2. We found that V_{oc} and FF can be further increased with increased Cl concentration. However, the J_{sc} decreases owing to the increased band gap.[45] The corresponding external quantum efficiency (EQE) is shown in Figure S9. The integrated current density from the EQE spectrum for PSCs based on $CsPb(I_{0.80}Br_{0.20})_3$:Cl and $CsPb(I_{0.67}Br_{0.33})_3$:Cl are 16.70 mA cm^{-2} and 14.44 mA cm^{-2}, respectively, which is comparable with the measured J_{sc} value. The small deviation of J_{sc} may originate from the perovskite film degradation under the high-humidity ambient testing environment for EQE. We also monitored the long-term stability including thermal stability (85°C) and illumination stability (0.8 sun) for $CsPb(I_{0.80}Br_{0.20})_3$, $CsPb(I_{0.80}Br_{0.20})_3$:Cl PSCs, $CsPb(I_{0.67}Br_{0.33})_3$, and $CsPb(I_{0.67}Br_{0.33})_3$:Cl PSCs over 250 h. The corresponding results are shown in Figure S12. Organic Spiro-OMeTAD material containing bis(trifluoromethane) sulfonimide lithium salt (Li-TFSI) and 4-*tert*-butylpyridine (TBP) is employed as a hole-transporting layer in our device, which could accelerate the degradation of the device under long-term thermal conditions due to the volatilization of the organic component. We also noted an increase in device performance under continuous illumination. We attribute this to the "light-soaking effect" as a possible mechanism.[46] For all-inorganic $CsPbX_3$ perovskite, vacancies traps such as V_I exist within the film. Ion migration could be initiated upon the illumination and the traps could be filled by mobile ions. Therefore, the trap-assisted recombination process could be suppressed, improving the performance after light soaking. The $CsPb(I_{0.80}Br_{0.20})$:Cl device exhibits better stability than the $CsPb(I_{0.67}Br_{0.33})$:Cl device. We attribute this to the higher perovskite film quality of the 20% Br perovskite. It was reported that grain boundaries as well as surface traps could provide a large number of channels for moisture and heat corrosion and cause the degradation of perovskite film.[47] The 20% Br perovskite exhibits better film quality with larger grains and fewer grain boundaries compared with the 33% Br perovskite, contributing to enhanced stability.

To further understand the enhancement of V_{oc} and FF, we performed steady-state photoluminescence (PL) (Figure 6D) and time-resolved PL (TRPL) (Figure 6E) to investigate the carrier recombination behaviors.[48] The incorporation of Cl could lead to extended carrier lifetime with enhanced steady-state PL intensity, implying a prolonged carrier diffusion length and reduced non-radiative recombination.[49] The blue-shift of emission spectra for the film with Cl is consistent with the UV-vis results. The time constants obtained by fitting TRPL results with a biexponential function are summarized in Table S3. The ideality factor (A) and series resistance (R_s) were evaluated according to the p-i-n diode model based on single heterojunction solar cells to reveal the electrical recombination mechanism (Figure 6F).[50] The plots of $-dV/dJ$ versus $(J_{sc} - 1)^{-1}$ and linear fitting curves of the PSCs with and without Cl films are depicted in Figure 6F. The values of R_s and A can be calculated from the intercept and slope of the linear fitting results.[51] After introducing Cl, the device exhibits smaller R_s and an A value closer to 1, suggesting that a well-behaved heterojunction with reduced non-radiative carrier recombination is formed.[52] We have also estimated the defect trap states by conducting dark current-voltage (I-V) analysis

(Figure S14). The inset image displays the electron-only device structure. The trap-filled limit voltage (V_{TFL}) is proportional to trap-state density (n_t), obtained from the intersection in the *I-V* curve. It is obvious that the perovskite film with Cl exhibits a lower trap-state density than that of perovskite film without Cl, confirming that Cl plays an important role in improving the film quality and suppressing the traps.

Conclusion

In conclusion, we disclosed the various crystallization pathways for all-inorganic perovskites $CsPbX_3$ (X = I, Br, and Cl) with different halide compositions by *in situ* GIWAXS. We found that the Br component can regulate the crystallization kinetics and thus affect the formation of the film. Besides, Br promoted the photoactive (black) phase formation and suppressed the unwanted yellow phase transition. An appropriate nucleation and crystallization process plays an important role in controlling the film morphology. Further introduction of Cl affords improved crystallinity and orientational order within the bulk film, contributing to longer charge-carrier lifetime and suppressed non-radiative recombination. With the assistance of Cl doping, the champion PSCs based on the conventional I/Br ratio of 2:1 yields a PCE of 15.02% under reverse voltage scanning. Remarkably, the optimized composition is found to be $CsPb(I_{0.8}Br_{0.2})_3$:Cl, which exhibits the largest grain size with compact film coverage, and thereby a record PCE of 17.14% with the smallest V_{oc} energy loss of 0.6 eV under reverse voltage scanning. To the best of our knowledge, this is the best PCE reported so far for all-inorganic PSCs using pure all-inorganic perovskite precursors without the assistance of organic additives. With a deep understanding of the film-formation kinetics revealed by *in situ* GIWAXS characterization, we not only demonstrated the power of ternary halide engineering to obtain high-performance all-inorganic PSCs with high-quality films and enhanced phase stability, but also provided guidelines for the future design of compositional engineering strategies.

EXPERIMENTAL PROCEDURES

Resource Availability

Lead Contact

Further information and requests for resources should be directed to and will be fulfilled by the Lead Contact, Xinhui Lu (xinhui.lu@cuhk.edu.hk).

Materials Availability

This study did not generate new or unique reagents.

Data and Code Availability

All experimental data are available upon reasonable request to the Lead Contact.

Materials

All reagents were used as received without further purification. Zn $(CH_3COO)_2 \cdot 2H_2O$, 2-methoxyethanol, and ethanolamine were obtained from J&K Scientific. CsI, PbI_2, $PbBr_2$, $PbCl_2$, anhydrous DMF, DMSO, isopropanol, acetonitrile, TBP, and Li-TFSI were purchased from Sigma-Aldrich. Spiro-OMeTAD was purchased from Ying Kou You Xuan.

Device Fabrications

Glass/ITO substrates (1.5 cm × 1.5 cm) was sequentially cleaned by sonication in detergent, deionized water, acetone, and ethanol, and dried with an N_2 blow gun before use. ZnO precursor was prepared by dissolving the 100 mg $Zn(CH_3COO)_2{\cdot}H_2O$ and 28.29 μL of ethanolamine in 973 μL of 2-methoxyethanol.The dissolved ZnO precursor was spin-coated onto the ITO substrates with a

spin rate of 4,000 rpm for 30s, followed by annealing for 30 min at 200°C. The $CsPb(I_{1-x}Br_x)_3$ (x = 0%, 20%, 33%, 50%, 66%) perovskite precursor was prepared by dissolving CsI, PbI_2, and $PbBr_2$ with desired I/Br rate in mixed solvent DMSO and DMF (6:4, v/v). The perovskite precursor solutions of $CsPbI_3$, $CsPb(I_{0.8}Br_{0.2})_3$, $CsPb(I_{0.67}Br_{0.33})_3$, $CsPb(I_{0.5}Br_{0.5})_3$, and $CsPb(I_{0.34}Br_{0.66})_3$ were spin-coated on ZnO substrate and annealed on a hotplate for 10 min. The $CsPbICl_2$ solution was obtained by dissolving 0.2 M CsI and $PbCl_2$ in mixed solvent DMSO and DMF (6:4, v/v), then added into the $CsPb(I_{1-x}Br_x)_3$ (x = 20%, 33%) precursor to obtain the desired Cl additive concentration. Hole-transporting material was deposited from a precursor composed of 72.3 mg of Spiro-OMeTAD, 28.8 μL of TBP, and 28.8 μL of FK209 (300 mg in 1 mL of acetonitrile and 17.5 μL of Li-TFSI solution [520 mg in 1 mL of acetonitrile]) in 1 mL of chlorobenzene. The Spiro-OMeTAD HTL was spun on the perovskite film at 5,000 rpm for 30 s. Finally, a 70-nm Au electrode contact layer was deposited by thermal evaporation.

Materials Characterizations

GIWAXS is a powerful technique for unveiling the evolution of the crystal growth kinetics process and phase-transition pathways of perovskite film. Brilliant synchrotron X-rays shining on the sample surface with a small angle below 2° of incidence excludes disturbance from strong background signal. The Bragg diffraction signals are collected by a 2-dimensional (2D) detector, which reveals the orientation and crystal structure information of the samples. The *ex situ* GIWAXS measurements were performed with a Xeuss 2.0 SAXS/WAXS laboratory beamline using a Cu X-ray source (8.05 keV, 1.54 Å) and a Pilatus3R 300K detector. The incidence angle was 0.3°. The measurement process was conducted in a vacuum chamber. The *in situ* GIWAXS measurements were carried out at the National Synchrotron Radiation Research Center (NSRRC), Hsinchu, Taiwan. Small and wide-angle X-ray scattering (SWAXS) X-rays with wavelength of 1.240 Å (10 keV) were used to irradiate the sample. The scattering signals were collected by a C9728DK area detector. The lanthanum hexaboride (LaB6) sample was used to calibrate. The incidence angle was kept at 2° to enhance the signal resolution with a frame exposure time of 3 s. *In situ* GIWAXS characterization was carried out during the film formation of $CsPb(I_{1-x}Br_x)_3$ (x = 0%, 20%, 33%, 50%, 66%) during the spin-coating process. The spin-coating process was conducted in a N_2-filled chamber at designated times during the whole 300-s spinning process at 1,500 rpm. GIWAXS measurement and sample spinning could be triggered simultaneously.

For the thermal stability test, the devices are put on a hotplate with 85°C under N_2 environment. For the illumination stability test, the devices are exposed under white LED arrays with 0.8-sun illumination intensity in a N_2-filled chamber. We clarify the detailed conditions and methods of stability testing in Supplemental Information.

The current density-voltage (*J-V*) curves were conducted in nitrogen by a Keithley 2400 source meter unit under an AM 1.5G solar simulator (100 mW cm^{-2}). The electrode area was 0.0475 cm^2. UV-vis absorption spectra were produced by a Hitachi U-3501 UV/visible/NIR spectrophotometer. Steady-state photoluminescence (PL) and time-resolved photoluminescence decay spectra were observed with a 485-nm laser (Horiba Jobin Yvon IBH). The crystalline structures of the prepared perovskite films were measured by XRD (Rigaku, Smart Lab). High-resolution field-emission SEM (FEI, Quanta 400) was performed to obtain the SEM images of the perovskite films. UV-vis absorption, PL, and XRD were conducted in ambient conditions with very low moisture (<40% relative humidity). There was no obvious degradation of the sample during the brief measurement process. The perovskite precursor solution of $CsPb(I_{1-x}Br_x)_3$

(x = 0%, 20%, 33%, 50%, 66%) were spin-coated on ZnO substrate and annealed on a hotplate at 160°C for 10 min. XPS characterization of the prepared perovskite films was measured at BL09A2 U5 beamline at the NSRRC, Taiwan, with an incident photon energy of 750 eV. Before testing the samples, an Au sample was used to calibrate the standard deviation. The reference binding energies (eV) (Mg Kα) of Au ($4f_{7/2}$) is 84.00 eV. The trap states were estimated by analyzing the dark current-voltage (*I-V*) based on electron-only devices with the structure of ITO/ZnO/perovskite/PCBM/Ag. The trap-filled limit voltage V_{TFL} can be determined by Equation 1, where *e* is the elementary charge of the electron, *L* is the thickness of the perovskite film, ϵ is the relative dielectric constant of perovskite, ϵ_0 is the vacuum permittivity, and n_t is the trap-state density. The V_{TFL} is proportional to n_t.

$$V_{TFL} = \frac{en_tL^2}{2\epsilon\epsilon_0} \quad \text{(Equation 1)}$$

SUPPLEMENTAL INFORMATION

Supplemental Information can be found online at https://doi.org/10.1016/j.matt.2020.10.023.

ACKNOWLEDGMENTS

The authors are grateful for the beam time and technical support provided by the 23A SWAXS beamline at NSRRC, Hsinchu. The authors acknowledge the financial support from Research Grant Council of Hong Kong (RGC) (General Research Fund no. 24306318, CUHK direct grant nos. 4053347 and 4055119), the National Natural Science Foundation of China (grant no. 11674252), and the Natural Science Foundation of Hubei Province, China (grant no. 2019AAA020).

AUTHOR CONTRIBUTIONS

Conceptualization, J.M. and M.Q.; Methodology, J.M. and M.Q.; Investigation, J.M. and M.Q.; Resources, J.M., M.Q., Y.L., X.W., Z.Q., and W.Y.; Writing – Original Draft, J.M. and M.Q.; Writing – Review & Editing, all authors; Supervision, G.F. and X.L.

DECLARATION OF INTERESTS

The authors declare no competing interests.

Received: July 4, 2020
Revised: October 13, 2020
Accepted: October 17, 2020
Published: November 11, 2020

REFERENCES

1. Jiang, Q., Zhao, Y., Zhang, X., Yang, X., Chen, Y., Chu, Z., Ye, Q., Li, X., Yin, Z., and You, J. (2019). Surface passivation of perovskite film for efficient solar cells. Nat. Photonics *13*, 460–466.

2. National Renewable Energy Laboratory (2020). Best Research-Cell Efficiency Chart. http://www.nrel.gov/pv/cell-efficiency.html.

3. Park, B.W., and Seok, S.I. (2019). Intrinsic instability of inorganic-organic hybrid halide perovskite materials. Adv. Mater. *31*, e1805337.

4. Zhang, J., Hodes, G., Jin, Z., and Liu, S.F. (2019). All-inorganic $CsPbX_3$ perovskite solar cells: progress and prospects. Angew. Chem. Int. Ed. *58*, 15596–15618.

5. Sutton, R.J., Eperon, G.E., Miranda, L., Parrott, E.S., Kamino, B.A., Patel, J.B., et al. (2016). Bandgap-tunable cesium lead halide perovskites with high thermal stability for efficient solar cells. Adv. Energy Mater. *6*, 1502458, https://doi.org/10.1002/aenm.201502458.

6. Wang, Z., Song, Z., Yan, Y., Liu, S.F., and Yang, D. (2019). Perovskite-a perfect top cell for tandem devices to break the S-Q limit. Adv. Sci. *6*, 1801704, https://doi.org/10.1002/advs.201801704.

7. Wang, P., Zhang, X., Zhou, Y., Jiang, Q., Ye, Q., Chu, Z., et al. (2018b). Solvent-controlled growth of inorganic perovskite films in dry environment for efficient and stable solar cells. Nat. Commun. *9*, 2225, https://doi.org/10.1038/s41467-018-04636-4.

8. Liao, J.-F., Rao, H.-S., Chen, B.-X., Kuang, D.-B., and Su, C.-Y. (2017). Dimension engineering on cesium lead iodide for efficient and stable perovskite solar cells. J. Mater. Chem. A *5*, 2066–2072.

9. Marronnier, A., Roma, G., Boyer-Richard, S., Pedesseau, L., Jancu, J.-M., Bonnassieux, Y., et al. (2018). Anharmonicity and Disorder in the Black Phases of Cesium Lead Iodide Used for Stable Inorganic Perovskite Solar Cells. ACS Nano *12*, 3477–3486.

10. Zhang, S., Wu, S., Chen, W., Zhu, H., Xiong, Z., Yang, Z., Chen, C., Chen, R., Han, L., and Chen, W. (2018). Solvent engineering for efficient inverted perovskite solar cells based on inorganic $CsPbI_2Br$ light absorber. Mater. Today Energy *8*, 125–133.

11. Chen, W., Chen, H., Xu, G., Xue, R., Wang, S., Li, Y., and Li, Y. (2019). Precise control of crystal growth for highly efficient $CsPbI_2Br$ perovskite solar cells. Joule *3*, 191–204.

12. Jiang, H., Feng, J., Zhao, H., Li, G., Yin, G., Han, Y., et al. (2018). Low temperature fabrication for high performance flexible $CsPbI_2Br$ perovskite solar cells. Adv. Sci. *5*, 1801117, https://doi.org/10.1002/advs.201801117.

13. Liu, Z., Meng, K., Wang, X., Qiao, Z., Xu, Q., Li, S., Cheng, L., Li, Z., and Chen, G. (2020). In situ observation of vapor-assisted 2D-3D heterostructure formation for stable and efficient perovskite solar cells. Nano Lett. *20*, 1296–1304.

14. Szostak, R., Marchezi, P.E., Marques, A.d.S., da Silva, J.C., de Holanda, M.S., Soares, M.M., Tolentino, H.C.N., and Nogueira, A.F. (2019). Exploring the formation of formamidinium-based hybrid perovskites by antisolvent methods: in situ GIWAXS measurements during spin coating. Sustain. Energy Fuels *3*, 2287–2297.

15. Fan, Y., Fang, J., Chang, X., Tang, M.-C., Barrit, D., Xu, Z., Jiang, Z., Wen, J., Zhao, H., Niu, T., et al. (2019). Scalable ambient fabrication of high-performance $CsPbI_2Br$ solar cells. Joule *3*, 2485–2502.

16. Qin, M., Tse, K., Lau, T.K., Li, Y., Su, C.J., Yang, G., et al. (2019). Manipulating the mixed-perovskite crystallization pathway unveiled by in situ GIWAXS. Adv. Mater. *31*, e1901284, https://doi.org/10.1002/adma.201901284.

17. Garcia-Fernandez, A., Bermudez-Garcia, J.M., Castro-Garcia, S., Llamas-Saiz, A.L., Artiaga, R., Lopez-Beceiro, J., Hu, S., Ren, W., Stroppa, A., Sanchez-Andujar, M., et al. (2017). Phase transition, dielectric properties, and ionic transport in the $[(CH_3)_2NH_2]PbI_3$ organic-inorganic hybrid with 2H-hexagonal perovskite structure. Inorg. Chem. *56*, 4918–4927.

18. Steele, J.A., Jin, H., Dovgaliuk, I., Berger, R.F., Braeckevelt, T., Yuan, H., et al. (2019). Thermal unequilibrium of strained black $CsPbI_3$ thin films. Science *365*, 679, https://doi.org/10.1126/science.aax3878.

19. Jena, A.K., Kulkarni, A., Sanehira, Y., Ikegami, M., and Miyasaka, T. (2018). Stabilization of α-$CsPbI_3$ in ambient room temperature conditions by incorporating Eu into $CsPbI_3$. Chem. Mater. *30*, 6668–6674.

20. Tian, J., Wang, J., Xue, Q., Niu, T., Yan, L., Zhu, Z., et al. (2020). Composition engineering of all-inorganic perovskite film for efficient and operationally stable solar cells. Adv. Funct. Mater. *30*, 2001764, https://doi.org/10.1002/adfm.202001764.

21. Sutton, R.J., Filip, M.R., Haghighirad, A.A., Sakai, N., Wenger, B., Giustino, F., and Snaith, H.J. (2018). Cubic or orthorhombic? Revealing the crystal structure of metastable black-phase $CsPbI_3$ by theory and experiment. ACS Energy Lett. *3*, 1787–1794.

22. Wang, K., Jin, Z., Liang, L., Bian, H., Bai, D., Wang, H., et al. (2018a). All-inorganic cesium lead iodide perovskite solar cells with stabilized efficiency beyond 15%. Nat. Commun. *9*, 4544, https://doi.org/10.1038/s41467-018-06915-6.

23. Swarnkar, A., Mir, W.J., and Nag, A. (2018). Can B-site doping or alloying improve thermal- and phase-stability of all-inorganic $CsPbX_3$ (X = Cl, Br, I) perovskites? ACS Energy Lett. *3*, 286–289.

24. Zhou, Y., and Zhao, Y. (2019). Chemical stability and instability of inorganic halide perovskites. Energy Environ. Sci. *12*, 1495–1511.

25. Wang, K., Jin, Z., Liang, L., Bian, H., Wang, H., Feng, J., and Liu, S. (Frank). (2019). Chlorine doping for black γ-$CsPbI_3$ solar cells with stabilized efficiency beyond 16%. Nano Energy *58*, 1175–1182.

26. Hieulle, J., Wang, X., Stecker, C., Son, D.Y., Qiu, L., Ohmann, R., Ono, L.K., Mugarza, A., Yan, Y., and Qi, Y. (2019). Unraveling the impact of halide mixing on perovskite stability. J. Am. Chem. Soc. *141*, 3515–3523.

27. Fan, L., Ding, Y., Luo, J., Shi, B., Yao, X., Wei, C., Zhang, D., Wang, G., Sheng, Y., Chen, Y., et al. (2017). Elucidating the role of chlorine in perovskite solar cells. J. Mater. Chem. A. *5*, 7423–7432.

28. Cheng, R., Chung, C.C., Zhang, H., Liu, F., Wang, W.T., Zhou, Z., et al. (2019). Tailoring triple-anion perovskite material for indoor light harvesting with restrained halide segregation and record high efficiency beyond 36%. Adv. Energy Mater. *9*, 1901980, https://doi.org/10.1002/aenm.201901980.

29. Lau, C.F.J., Wang, Z., Sakai, N., Zheng, J., Liao, C.H., Green, M., et al. (2019). Fabrication of efficient and stable $CsPbI_3$ perovskite solar cells through cation exchange process. Adv.Energy Mater. *9*, 101685, https://doi.org/10.1002/aenm.201901685.

30. Ye, Q., Zhao, Y., Mu, S., Ma, F., Gao, F., Chu, Z., et al. (2019). Cesium lead inorganic solar cell with efficiency beyond 18% via reduced charge recombination. Adv. Mater. *31*, e1905143, https://doi.org/10.1002/adma.201905143.

31. Wang, Y., Zhang, T., Kan, M., and Zhao, Y. (2018c). Bifunctional stabilization of all-inorganic alpha-$CsPbI_3$ perovskite for 17% efficiency photovoltaics. J. Am. Chem. Soc. *140*, 12345–12348.

32. Meng, H., Shao, Z., Wang, L., Li, Z., Liu, R., Fan, Y., Cui, G., and Pang, S. (2019). Chemical composition and phase evolution in DMAI-derived inorganic perovskite solar cells. ACS Energy Lett. *5*, 263–270.

33. Chen, H., Xiang, S., Li, W., Liu, H., Zhu, L., and Yang, S. (2018). Inorganic perovskite solar cells: a rapidly growing field. Solar RRL *2*, 1700188, https://doi.org/10.1002/solr.201700188.

34. Straus, D.B., Guo, S., Abeykoon, A.M., and Cava, R.J. (2020). Understanding the instability of the halide perovskite $CsPbI_3$ through temperature-dependent structural analysis. Adv. Mater. *32*, e2001069, https://doi.org/10.1002/adma.202001069.

35. Liang, L., Li, Z., Zhou, F., Wang, Q., Zhang, H., Xu, Z., Ding, L., Liu, S., and Jin, Z. (2019). The humidity-insensitive fabrication of efficient $CsPbI_3$ solar cells in ambient air. J. Mater. Chem. A *7*, 26776–26784.

36. Gao, L., and Yang, G. (2019). Organic-inorganic halide perovskites: from crystallization of polycrystalline films to solar cell applications. Solar RRL *4*, 1900200, https://doi.org/10.1002/solr.201900200.

37. Nam, J.K., Chun, D.H., Rhee, R.J.K., Lee, J.H., and Park, J.H. (2018). Methodologies toward efficient and stable cesium lead halide perovskite-based solar cells. Adv. Sci. *5*, 1800509, https://doi.org/10.1002/advs.201800509.

38. Ono, L.K., Juarez-Perez, E.J., and Qi, Y. (2017). Progress on perovskite materials and solar cells with mixed cations and halide anions. ACS Appl. Mater. Interfaces *9*, 30197–30246.

39. Jiang, F., Rong, Y., Liu, H., Liu, T., Mao, L., Meng, W., et al. (2016). Synergistic effect of PbI_2 Passivation and chlorine inclusion yielding high open-circuit voltage exceeding 1.15 V in both mesoscopic and inverted planar $CH_3NH_3PbI_3(Cl)$-Based perovskite solar cells. Adv. Funct. Mater. *26*, 8119–8127.

40. Ma, J., Li, Y., Li, J., Qin, M., Wu, X., Lv, Z., Hsu, Y.-J., Lu, X., Wu, Y., and Fang, G. (2020). Constructing highly efficient all-inorganic perovskite solar cells with efficiency exceeding 17% by using dopant-free polymeric electron-donor materials. Nano Energy *75*, 104933.

41. Yan, L., Xue, Q., Liu, M., Zhu, Z., Tian, J., Li, Z., et al. (2018). Interface engineering for all-inorganic $CsPbI_2Br$ perovskite solar cells with efficiency over 14. Adv. Mater. *30*, e1802509, https://doi.org/10.1002/adma.201802509.

42. Ma, J., Qin, M., Li, Y., Zhang, T., Xu, J., Fang, G., and Lu, X. (2019). Guanidinium doping enabled low-temperature fabrication of high-efficiency all-inorganic $CsPbI_2Br$ perovskite solar cells. J. Mater. Chem. A *7*, 27640–27647.

43. Zeng, Q., Zhang, X., Feng, X., Lu, S., Chen, Z., Yong, X., et al. (2018). Polymer-passivated inorganic cesium lead mixed-halide perovskites for stable and efficient solar cells with high open-circuit voltage over 1.3 V. Adv. Mater. *30*, 1705393, https://doi.org/10.1002/adma.201705393.

44. Luo, D., Su, R., Zhang, W., Gong, Q., and Zhu, R. (2019). Minimizing non-radiative recombination losses in perovskite solar cells. Nat. Rev. Mater. *5*, 44–60.

45. Stone, K.H., Gold-Parker, A., Pool, V.L., Unger, E.L., Bowring, A.R., McGehee, M.D., et al. (2018). Transformation from crystalline precursor to perovskite in $PbCl_2$-derived $MAPbI_3$. Nat. Commun. https://doi.org/10.1038/s41467-018-05937-4.

46. Shao, S., Abdu-Aguye, M., Sherkar, T.S., Fang, H.-H., Adjokatse, S., Brink, G.t., Kooi, B.J., Koster, L.J.A., and Loi, M.A. (2016). The effect of the microstructure on trap-assisted recombination and light soaking phenomenon

in hybrid perovskite solar cells. Adv. Funct. Mater. *26*, 8094–8102.

47. Zhang, H., Shi, J., Zhu, L., Luo, Y., Li, D., Wu, H., and Meng, Q. (2018). Polystyrene stabilized perovskite component, grain and microstructure for improved efficiency and stability of planar solar cells. Nano Energy *43*, 383–392.

48. Bai, F., Zhang, J., Yuan, Y., Liu, H., Li, X., Chueh, C.C., et al. (2019). A 0D/3D heterostructured all-inorganic halide perovskite solar cell with high performance and enhanced phase stability. Adv. Mater. *31*, 1904735, https://doi.org/10.1002/adma.201904735.

49. Tong, G., Chen, T., Li, H., Qiu, L., Liu, Z., Dang, Y., Song, W., Ono, L.K., Jiang, Y., and Qi, Y. (2019). Phase transition induced recrystallization and low surface potential barrier leading to 10.91%-efficient $CsPbBr_3$ perovskite solar cells. Nano Energy *65*, 104015.

50. Shi, J., Dong, J., Lv, S., Xu, Y., Zhu, L., Xiao, J., et al. (2014). Hole-conductor-free perovskite organic lead iodide heterojunction thin-film solar cells: high efficiency and junction property. Appl. Phys. Lett. *104*, https://doi.org/10.1063/1.4864638.

51. Ma, J., Yang, G., Qin, M., Zheng, X., Lei, H., Chen, C., et al. (2017). MgO nanoparticle modified anode for highly efficient SnO_2-based planar perovskite solar cells. Adv. Sci. *4*, 1700031, https://doi.org/10.1002/advs.329.

52. Ma, J., Zheng, M., Chen, C., Zhu, Z., Zheng, X., Chen, Z., et al. (2018). Efficient and stable nonfullerene-graded heterojunction inverted perovskite solar cells with inorganic Ga_2O_3Tunneling protective nanolayer. Adv. Funct. Mater. *28*, 1804128, https://doi.org/10.1002/adfm.201804128.